Geophysical Journal International

Geophys. J. Int. (2010) **180,** 765–780 doi: 10.1111/j.1365-246X.2009.04436.x

Variations of the velocity contrast and rupture properties of M6 earthquakes along the Parkfield section of the San Andreas fault

Peng Zhao,[1] Zhigang Peng,[1] Zheqiang Shi,[2] Michael A. Lewis[2] and Yehuda Ben-Zion[2]

[1] *School of Earth and Atmospheric Sciences, Georgia Institute of Technology, Atlanta,* GA 30332*, USA. E-mail: pzhao@gatech.edu*
[2] *Department of Earth Sciences, University of Southern California, Los Angeles,* CA 90089-0740*, USA*

Accepted 2009 October 28. Received 2009 July 26; in original form 2009 February 1

SUMMARY

We investigate the seismic velocity contrast across the San Andreas fault (SAF) in the Parkfield area using fault zone head waves (FZHW) that propagate along the bimaterial fault interface and direct *P* waves. We systematically analyse large data sets of near-fault waveforms recorded by several seismic networks over the period 1984–2005. Clear FZHW are observed at many stations on the NE side of the fault in the creeping section of the SAF north of Middle Mountain (MM). This indicates the presence of a sharp bimaterial interface and that the NE side of the fault has lower seismic velocities in that region. The obtained *P*-wave velocity contrast is about 5–10 per cent north of MM, and it systematically decreases to 0–2 per cent near Gold Hill (GH). The along-strike variations of the velocity contrast are consistent with geological observations of a sliver of high-velocity rock immediately to the NE of the SAF near GH, associated with the GH fault, and existing 3-D seismic tomography results. The obtained imaging results offer an explanation for the mixed rupture directions of the M6-type Parkfield earthquakes. The strong velocity contrast around MM is expected to produce a preferred propagation direction to the SE for earthquakes that nucleate near MM (e.g. the 1934 and 1966 Parkfield earthquakes). In contrast, the near-zero velocity contrast and multiple fault branches near GH imply that earthquakes that nucleate near GH (e.g. the 2004 Parkfield earthquake) are not expected to have a preferred propagation direction to the SE, and are likely to propagate in directions that are controlled by other factors such as structural and stress heterogeneities. The observed systematic reduction of the velocity contrast along the SAF from NW of MM to SE of GH provides a dynamic arrest mechanism for earthquakes that nucleate in the northern part of the Parkfield section and propagate to the SE, and a dynamic arrest mechanism for earthquakes that nucleate in the southern section and propagate to the NW.

Key words: Earthquake dynamics; Body waves; Earthquake interaction, forecasting and prediction; Interface waves; Rheology and friction of fault zones; Continental tectonics: strike-slip and transform.

1 INTRODUCTION

Large earthquakes occur on major fault structures. Due to long-term tectonic movements, such faults tend to juxtapose rocks of different elastic properties, resulting in well-defined bimaterial interfaces. Contrasts of elastic properties across large faults have been imaged by seismic reflection and refraction studies (e.g. Fuis *et al.* 2001, 2003; Catchings *et al.* 2002; Lutter *et al.* 2004), body and surface wave tomography (e.g. Eberhart-Phillips & Michael 1993; Shapiro *et al.* 2005; Thurber *et al.* 2006), modelling of geodetic data (Le Pichon *et al.* 2005; Fialko 2006; Wdowinski *et al.* 2007) and analysis of fault zone head waves (FZHW) that refract along the bimaterial fault interfaces (Ben-Zion & Malin 1991; Ben-Zion *et al.* 1992; Hough *et al.* 1994; McGuire & Ben-Zion 2005; Lewis *et al.* 2007; Zhao & Peng 2008).

Properties of earthquake ruptures on a bimaterial interface and associated seismic radiation can be significantly different from those expected for a fault in a homogenous solid (e.g. Weertman 1980; Andrews & Ben-Zion 1997; Ben-Zion 2001; Ranjith & Rice 2001). In contrast to the case of a homogenous solid, ruptures on a planar bimaterial interface produce dynamic changes of normal stress σ_n that depend on the spatial derivative of in-plane slip, material properties, rupture velocity, and the direction of rupture propagation. For standard subshear ruptures the change of σ_n at the tip propagating in the direction of slip of the compliant solid (referred to as the 'preferred' direction) is tensile, while the change at the tip

propagating in the opposite direction is compressive. For supershear ruptures, the senses of changes of σ_n are reversed (Weertman 2002; Shi & Ben-Zion 2006). The amplitudes of the near-tip changes increase with propagation distance along the bimaterial interface due to a continual transfer of energy to shorter wavelengths (e.g. Adams 1995; Ben-Zion & Huang 2002). The above dynamic effects produce a slip pulse that propagates for wide ranges of frictional, bimaterial contrast, and initial stress conditions predominately in the preferred direction (e.g. Shi & Ben-Zion 2006; Brietzke *et al.* 2007, 2009; Dalguer & Day 2007; Ampuero & Ben-Zion 2008). The seismic shaking hazard associated with earthquake ruptures depends strongly on the rupture direction (e.g. Aki & Richards 2002; Ben-Zion 2003; Olsen *et al.* 2006). The interaction between slip and normal traction along a bimaterial interface makes those interfaces mechanically-favored surfaces for rupture propagation (Ben-Zion & Andrews 1998; Brietzke & Ben-Zion 2006).

Many moderate and large earthquakes appear to be unilateral (McGuire *et al.* 2001). If the rupture propagation directions of earthquakes are affected strongly by the existence of bimaterial interfaces, the imaging of such interfaces can be used to predict a statistical preference for the propagation directions of earthquakes on the various structures. This knowledge can greatly improve the ability to evaluate local seismic risks and mitigate earthquake hazard. The seismic data associated with the well-instrumented Parkfield section of the San Andreas fault (SAF) in central California (e.g. Bakun *et al.* 2005) provide important opportunities for detailed examinations of the relations between fault zone structures and earthquake properties. The SAF in that area (Fig. 1) juxtaposes overall a faster granitic block on the SW side against a slower Franciscan block on the NE side, but the velocity structure is associated with various local complexities (e.g. Eberhart-Phillips & Michael 1993; Rymer *et al.* 2006; Thurber *et al.* 2006). The 1966 M6 Parkfield earthquake (and presumably several previous M6 events in the area) nucleated under Middle Mountain (MM) and propagated along the SAF towards the SE, while the 2004 M6 Parkfield earthquake started near Gold Hill (GH) and propagated primarily in the opposite direction (Bakun *et al.* 2005).

The 'opposite' propagation direction of the 2004 Parkfield event led Harris (2004) and Harris & Day (2005) to conclude that bimaterial interfaces are not important for earthquakes rupture on natural faults. Ben-Zion (2006) commented that the mixed propagation directions may be produced by local variations of the velocity structure associated with (1) a sliver of high-velocity rock immediately to the NE of the SAF, related to the GH fault, which may produce a local reversal of the velocity contrast near the hypocentre of the 2004 M6 event and (2) the existence of two major bimaterial interfaces—the main SAF and the Southwest Fracture Zone (SWFZ)—having velocity contrasts of opposite sense. Ben-Zion (2006) pointed out that higher resolution imaging studies of bimaterial interfaces, along with better statistics, are needed to test the hypothesis of preferred propagation direction of earthquake ruptures in the Parkfield area.

In this paper, we provide detailed seismic imaging of the velocity contrast across the SAF in the Parkfield area, by systematically analysing FZHW recorded by many near-fault seismic instruments. The results show systematic variations of the velocity contrast across the SAF that may help to explain the observed behaviour of moderate and large earthquakes in the area. In the next section, we describe the geological setting and previous studies of the velocity structures around Parkfield. In Section 3, we provide a brief review of FZHW signals and in Section 4 we describe details of the analysis procedure. The results are presented in Sections 5–7 and further discussed in Section 8.

2 TECTONIC SETTING AND PREVIOUS STUDIES OF VELOCITY STRUCTURES AROUND THE PARKFIELD SECTION OF THE SAF

The SAF is a right-lateral strike-slip fault that extends approximately 1200 km along the boundary between the Pacific and the North American plates. The Parkfield section of the SAF straddles the transition between the creeping segment of the fault to the NW and the locked segment to the SE that last ruptured in the great 1857 Fort Tejon earthquake (Sieh 1978). At least seven characteristic earthquakes of ∼M6 occurred at Parkfield since 1857, with the most recent one on 2004 September 28 (Bakun *et al.* 2005). The quasi-periodicity of the first six events led to the deployment of many seismic instruments as part of the Parkfield Earthquake Prediction Experiment (Bakun & Lindh 1985). The instrumentation was further augmented by the recent development of the SAFOD project (Hickman *et al.* 2004).

The surface geological setting around Parkfield is complicated. In general, the rock types in this section are characterized by faster Salinian granite on the SW side of the fault, and slower Franciscan rocks and Great Valley sequence on the NE side (Page 1981; Walter & Mooney 1982; Lees & Malin 1990). However, the near-fault seismic velocity structure includes numerous local variations (e.g. Eberhart-Phillips & Michael 1993; Thurber *et al.* 2006). In addition, the San Andreas system between MM and GH is expressed as two principal surface traces (Brown *et al.* 1967; Rymer *et al.* 2006): the main SAF and the SWFZ (Fig. 1). The main SAF surface trace shows a right-stepping offset across the Cholame Valley south of GH. This offset is considered to be the northern end of the locked segment that ruptured in the 1857 event, and responsible for bounding the southern rupture extents of the M6 Parkfield earthquakes (Lindh & Boore 1981).

While the detailed near-surface structures of the San Andreas system appear complicated, the relocated seismicity outlines a much simpler fault at seismogenic depth (Waldhauser *et al.* 2004; Thurber *et al.* 2006). The aftershocks of the 2004 Parkfield earthquake concentrate along the same locations associated with the pre-2004 seismicity, and form a linear trend that is directly beneath the SWFZ rather than the main SAF (Waldhauser *et al.* 2004; Simpson *et al.* 2006; Thurber *et al.* 2006). The seismicity trend connects to the creeping and locked sections of the SAF without obvious bends, suggesting that the SAF is expressed as a single planar fault at seismogenic depth (Eberhart-Phillips & Michael 1993; Thurber *et al.* 2006). Based on this and other geological observations, Simpson *et al.* (2006) suggested that the step-over and the wrapping of the main SAF to the NE is a consequence, rather than the cause, of the segmentation of the ∼M6 Parkfield earthquakes and the locked patch further south that last ruptured in the 1857 Fort Tejon earthquake.

Several local earthquake tomography models have been developed for a wide region around Parkfield (Lees & Malin 1990; Eberhart-Phillips & Michael 1993; Thurber *et al.* 2006), and a small region around MM (Michelini & McEvilly 1991; Thurber *et al.* 2003, 2004). A common feature among these models is a clear seismic velocity gradient across the SAF, with SW being overall fast and NE being overall slow, which is generally consistent with the geological observation at the surface. Ben-Zion & Malin (1991) observed FZHW at several stations on the NE side of the SAF, indicative of a sharp velocity contrast, and derived from the moveout between the head and direct *P* waves an average velocity contrast of about 5 per cent across the SAF near MM. Ben-Zion

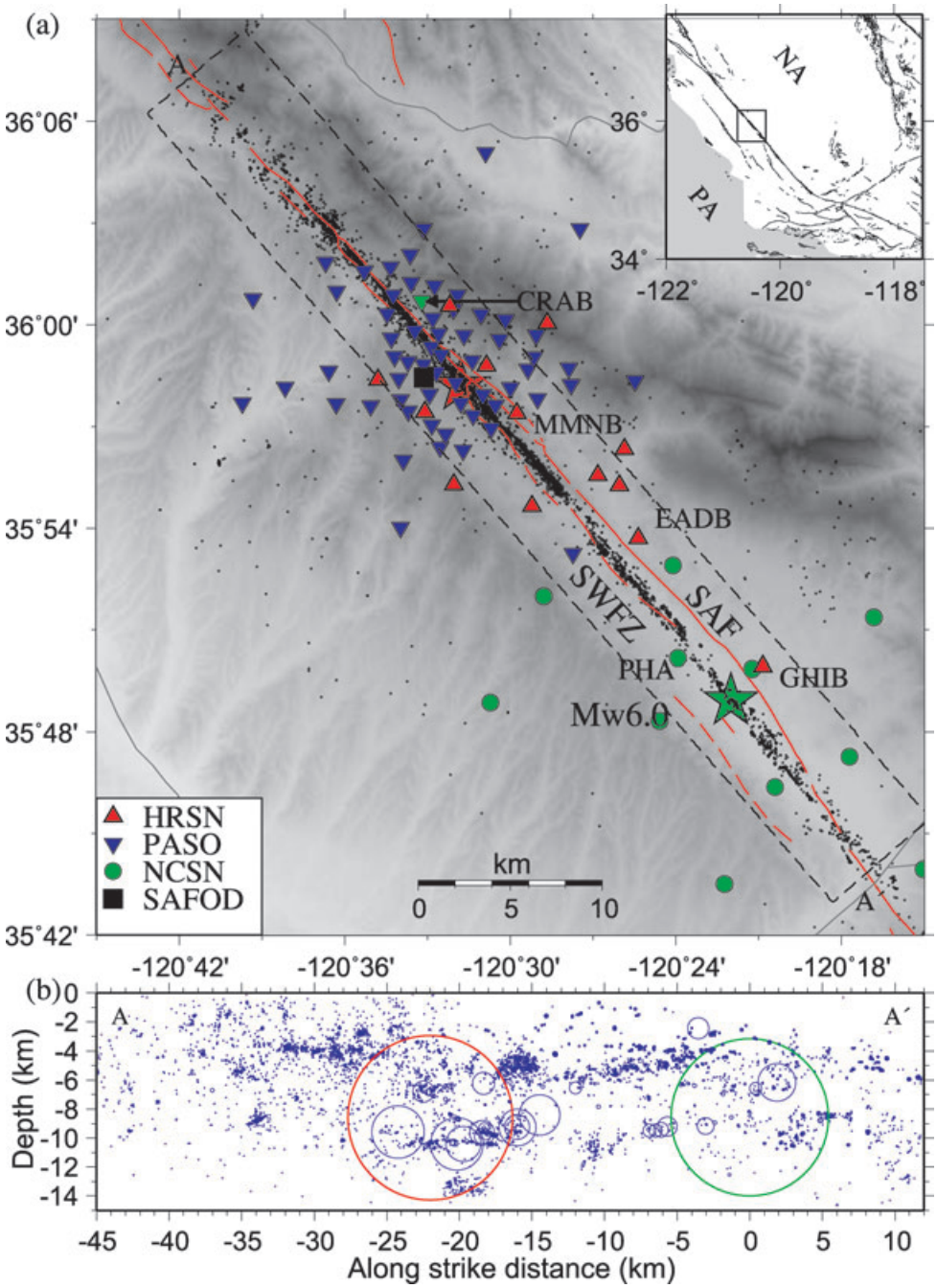

Figure 1. (a) A map of the Parkfield section of the San Andreas fault (SAF). The background seismicity from 1984 and 2005 (Thurber *et al.* 2006) and the epicentres of the 1966 and 2004 M6 Parkfield earthquakes are marked with small dots, and red and green stars, respectively. The red lines denote surface traces of faults. Seismic stations of several networks are shown with different symbols. Selective station names are marked. The background is shaded topography with white being low and dark being high. The inset shows the area on a map of California. SAF: the main San Andreas fault; SWFZ: Southwest Fracture Zone. (b) Hypocentres of about 9000 earthquakes inside the dashed box along the cross-section AA′ (139.2° strike) in (a). The radius of each circle is estimated from its magnitude, based on a moment-magnitude relationship (Abercrombie 1996) with a circular crack model (Eshelby 1957) assuming a nominal 3-MPa stress drop. The red and green circles mark the 1966 and 2004 M6 Parkfield earthquakes, respectively.

et al. (1992) inverted arrival times of FZHW and direct *P* waves for depth-variations of the velocity contrast near MM, and obtained values that range from 10 to 20 per cent in the top 3 km and 3–7 per cent in the deeper section.

Eberhart-Phillips & Michael (1993) and Thurber *et al.* (2006) imaged in tomography studies the existence of a high-velocity rock on the (nominally slow) NE side of the fault at seismogenic depth near GH (Fig. 2). This high-velocity body has a maximum *P*-wave velocity of 6.6 km s^{-1}, and is assumed to consist of the greenstones and mafic rocks of the Permanente Terrane (McLaughlin *et al.* 1996). Thurber *et al.* (2006) suggested that this high-velocity body is very close to or in contact with the SAF interface at depth, and might be spatially related to the area of primary slip (10 cm or more) during the 2004 Parkfield main shock (Langbein *et al.* 2005).

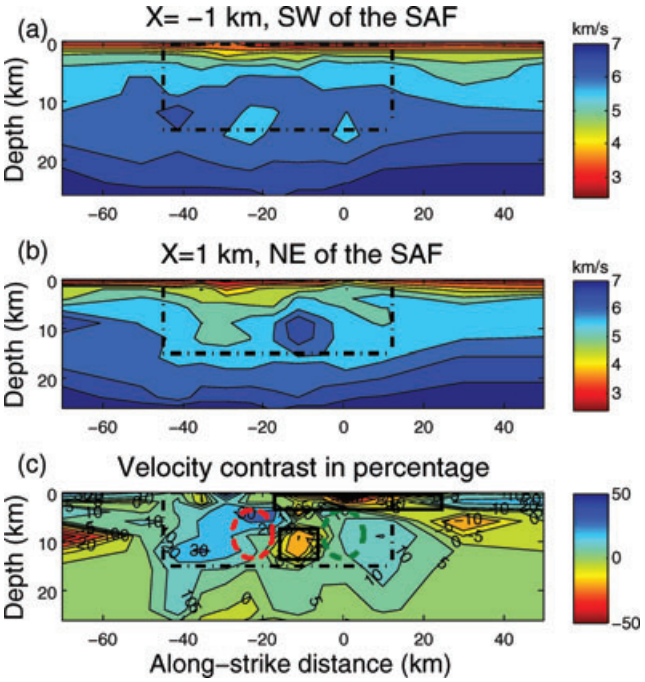

Figure 2. A velocity model from Thurber *et al.* (2006) at (a) $x = -1$ km, SW of the SAF and (b) $x = 1$ km, NE of the SAF. (c) The velocity contrast in percentage along the fault-strike and downdip directions, obtained by dividing the difference with the averaged velocities shown in (a) and (b). The positive number corresponds to faster velocity in the SW side. Two black rectangles roughly outline the two regions with reversed velocity contrast larger than 5 per cent (i.e. the NE side has faster velocity than the SW side). The red and green dashed circles mark, respectively, the hypocentres of the 1966 and 2004 Parkfield M6 events. The dashed black box corresponds to the region shown in Fig. 1(b).

3 SEISMIC FAULT ZONE HEAD WAVES

Unlike the aforementioned tomography studies that use traveltimes of the direct P and/or S waves to image properties of volumetric rock elements, we utilize FZHW to image directly the bimaterial interface along the Parkfield section of the SAF. A sharp material contrast across a fault interface should generate FZHW that spend a large portion of their propagation paths refracting along the bimaterial interface (Ben-Zion 1989, 1990; Ben-Zion & Aki 1990; Shi & Ben-Zion 2009). The FZHW propagate along the fault with the velocity and motion polarity of the block with faster seismic velocity. From the bimaterial interface, the FZHW are radiated to the side with slower velocity, where they are characterized by an emergent waveform with opposite motion polarity to that of the direct body wave. The FZHW are the first arriving phases at locations on the slower block with normal distance to the fault (Ben-Zion 1989) less than a critical distance x_c given by

$$x_c = r \cdot \tan\left[\cos^{-1}(\alpha_2/\alpha_1)\right], \tag{1}$$

where r is the distance that the FZHW propagate along the bimaterial interface and α_1, α_2 are the average P-wave velocities of the faster and slower media, respectively. Fig. 3 illustrates the relations between the velocity contrast and critical distance x_c for different along-fault distances r. For a given distance r, smaller values of the velocity contrast require stations that are closer to the fault to detect the FZHW. With known values of r and normal distances of stations

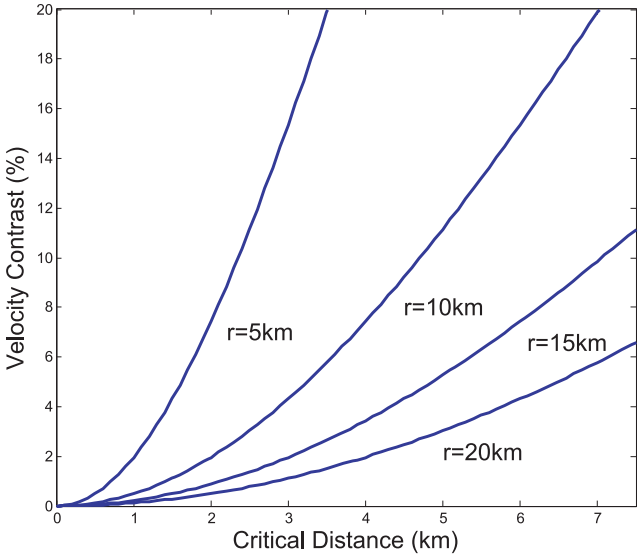

Figure 3. The critical normal distance from the fault x_c versus the value of velocity contrast as a function of along-fault propagation distance r using eq. (1). FZHW are the first arrivals for contrast values above the blue curves with different propagation distances r.

from the fault, Fig. 3 could be used to place limits on the velocity contrast, as done in Section 7 of the paper.

Since FZHW owe their existence to and spend most of their propagation paths along the fault interface, they provide a high-resolution tool for imaging the velocity contrast across the fault, as demonstrated in previous studies (e.g. Ben-Zion *et al.* 1992; McGuire & Ben-Zion 2005; Lewis *et al.* 2007; Zhao & Peng 2008). For an interface between two different quarter spaces, the differential arrival time (Δt) between first arriving head wave and the following direct P wave grows with r (Ben-Zion & Malin 1991) as

$$\Delta t \sim r\left(\frac{1}{\alpha_2} - \frac{1}{\alpha_1}\right) \sim r\left(\frac{\Delta\alpha}{\alpha^2}\right), \tag{2}$$

where α and $\Delta\alpha$ denote the average and differential P-wave velocities, respectively. In this study, we use eq. (2) to estimate along-strike variations of the velocity contrast in the Parkfield section of the SAF.

As mentioned, Ben-Zion & Malin (1991) and Ben-Zion *et al.* (1992) used head and direct P waves to image the velocity contrast across the SAF near MM. Ben-Zion *et al.* (1992) also demonstrated with numerical tests that including FZHW can significantly improve the resolution of the velocity structure near the fault. However, these studies only utilized a small data set associated with about 100 earthquakes NW of MM, and hence did not provide detailed images of the velocity contrast at different along-strike locations, and in particular around the epicentre of the 2004 Parkfield event near GH. In the following sections we conduct a comprehensive analysis of FZHW and P body waves for the velocity contrast across the SAF at different along-strike positions, using all the available relevant seismic data in the Parkfield area from 1984 to 2005.

4 DATA AND ANALYSIS PROCEDURE

The seismic data analysed in this study are recorded by two permanent networks, the Northern California Seismic Network (NCSN) operated by the USGS and the High Resolution Seismic Network (HRSN) operated by the Berkeley Seismological Laboratory (BSL), along with one temporary PASSCAL deployment, the Parkfield

Area Seismic Observatory (PASO) Network (Thurber *et al.* 2003). Most surface instruments (NCSN and PASO) are 1 Hz L4C or 2 Hz L22 short-period velocity sensors with a sampling rate of 100 s^{-1}. In the PASO network, 29 stations are equipped with Guralp 40T broadband instruments. The 13 HRSN 2 or 4.5 Hz short-period sensors are deployed in 100–300 m deep boreholes and have a sampling rate of 250 s^{-1}. In this study, we only analyse waveforms recorded by the vertical component. The hypocentre locations and origin times of earthquakes are obtained from the relocated catalogue of Thurber *et al.* (2006).

The employed analysis procedure is as follows. First, we select events occurring near the SAF. Because the majority of the seismicity in Parkfield appears as one linear trend beneath the surface traces of the SWFZ (Fig. 1), we only use events within 1 km of the linear seismicity trend. The strike of this trend is 139.2° clockwise from the North and we use the epicentre of the 2004 M6 event (−120.366°, 35.815°) listed in Thurber *et al.* (2006) as the projection centre. Next, we select high-quality waveforms with signal-to-noise ratio (SNR) ≥ 5 for the HRSN data. We use SNR ≥ 10 for the PASO and NCSN data because waveforms recorded by the surface stations are generally nosier than those from borehole instruments.

After the forgoing steps, we obtain about 2500 and 150 events for stations of the HRSN and PASO networks, respectively. This provides a good spatial coverage, especially around the epicentre of the 1966 Parkfield earthquake (i.e. MM). The distribution of seismic stations around the epicentre of 2004 Parkfield earthquake is relatively sparse. To balance the distribution of stations and seismicity, we select only 11 stations of the NCSN, which are located around the southern end of our study region near GH (Fig. 1). We use about 600 events for these 11 NCSN stations, ranging from 27 km north of the epicentre of the 2004 M6 event to the southern end of our study region.

After selecting waveforms with high SNR, we remove the mean value of each trace and apply a high-pass filter with a corner frequency of 1 Hz to suppress long period noise. Because the characteristics of FZHW are best expressed in displacement seismogram, we integrate the original velocity seismograms to obtain the displacement records, and pick the onset of FZHW and direct *P* waves manually by examining the velocity and displacement seismograms simultaneously. We identify FZHW as emergent first arrivals with opposite motion polarities and systematic moveout from the direct *P* waves. The onset of the *P* wave is picked at a place with a sharp increase of amplitude in the displacement seismogram (Ben-Zion 1989). Moreover, we require the polarities of direct *P* waves to be consistent with right-lateral focal mechanisms. This is justified by the fact that ∼75 per cent of the microseismicity at Parkfield are pure strike-slip events on the near-vertical planes aligned with the seismicity trend (Thurber *et al.* 2006; J. L. Hardebeck, written communication 2008). We also remove records with wrong polarities generated during certain operation periods of the stations.

Next, we assign three quality factors (A, B and C) to the picks of both FZHW and *P* waves. Quality A and C represent the highest and lowest confidence levels for phase picking, respectively, while Quality B is an intermediate level. The selection criteria are as follows. Phases with Quality A have both correct polarities based on right-lateral focal mechanisms and similar waveform characteristics as the synthetic solutions of the FZHW and *P* waves (Ben-Zion 1989, 1990). For stations on the NE of the SAF, the expected polarities of the direct *P* waves for events from the NW and SE along-strike directions are up and down, respectively. The direct *P* waves are expected to have strong sharp peaks/troughs, and the FZHW are expected to be emergent phases with opposite polarity from those of the direct *P* waves (Fig. 4a). Quality C is used when either the onset of FZHW/direct *P* wave is not reliable due to a low SNR value, or it is relatively difficult to determine the phase type because of waveform complexities. In Fig. 4(c), the polarity of the first-arriving phase is consistent with that of a FZHW for a right-lateral focal mechanism, but the complex waveform makes it difficult to pick the onset of the direct *P* phase. In such cases we set the qualities of both the FZHW and *P* wave to be C. In Fig. 4(b) the polarity of the first peak suggests that it is a head wave, assuming a right-lateral focal mechanism. However, its amplitude is at the same level as the later-arriving direct *P* phase and there is no sharp transition in the character of the two phases as in Quality A seismograms. Hence, we set the quality factors of both head wave and direct *P* arrival to be B. The selection of quality factors is somewhat subjective and relies on the experience of an analyst. To confirm the quality factor of each picked phase, we also check phases of nearby events and compare the results from different stations. The results presented in the following sections are based only on phase picks with quality A or B.

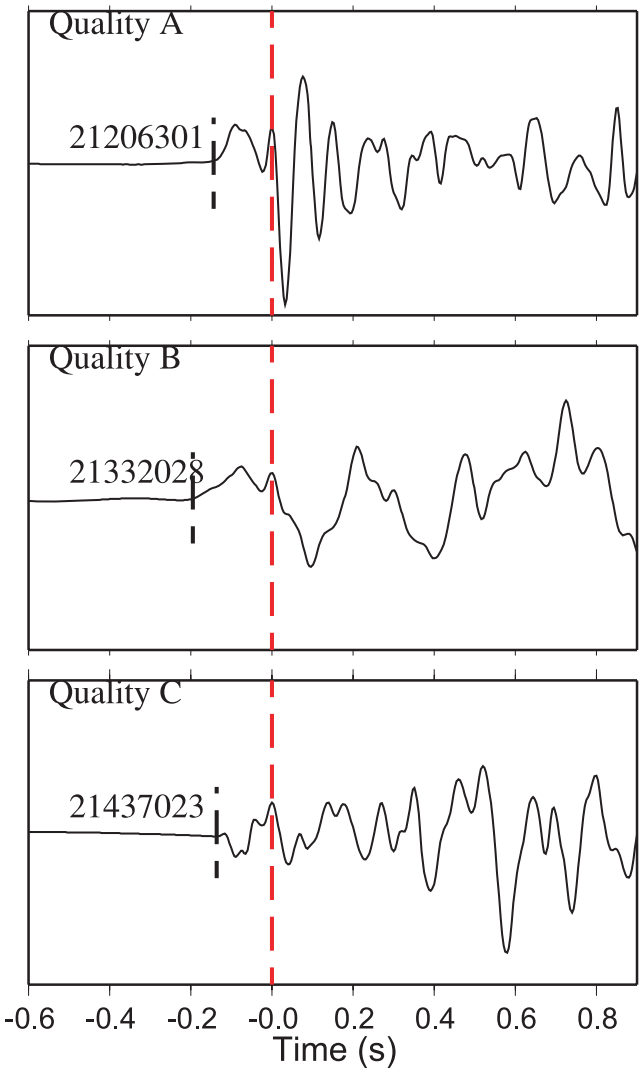

Figure 4. Examples of displacement waveforms recorded at station MMNB showing different qualities of the FZHW picks. The red and black vertical dashed lines mark the onsets of direct *P* waves and FZHW, respectively. The 8-digit numbers denote the CUSP id of the corresponding waveforms.

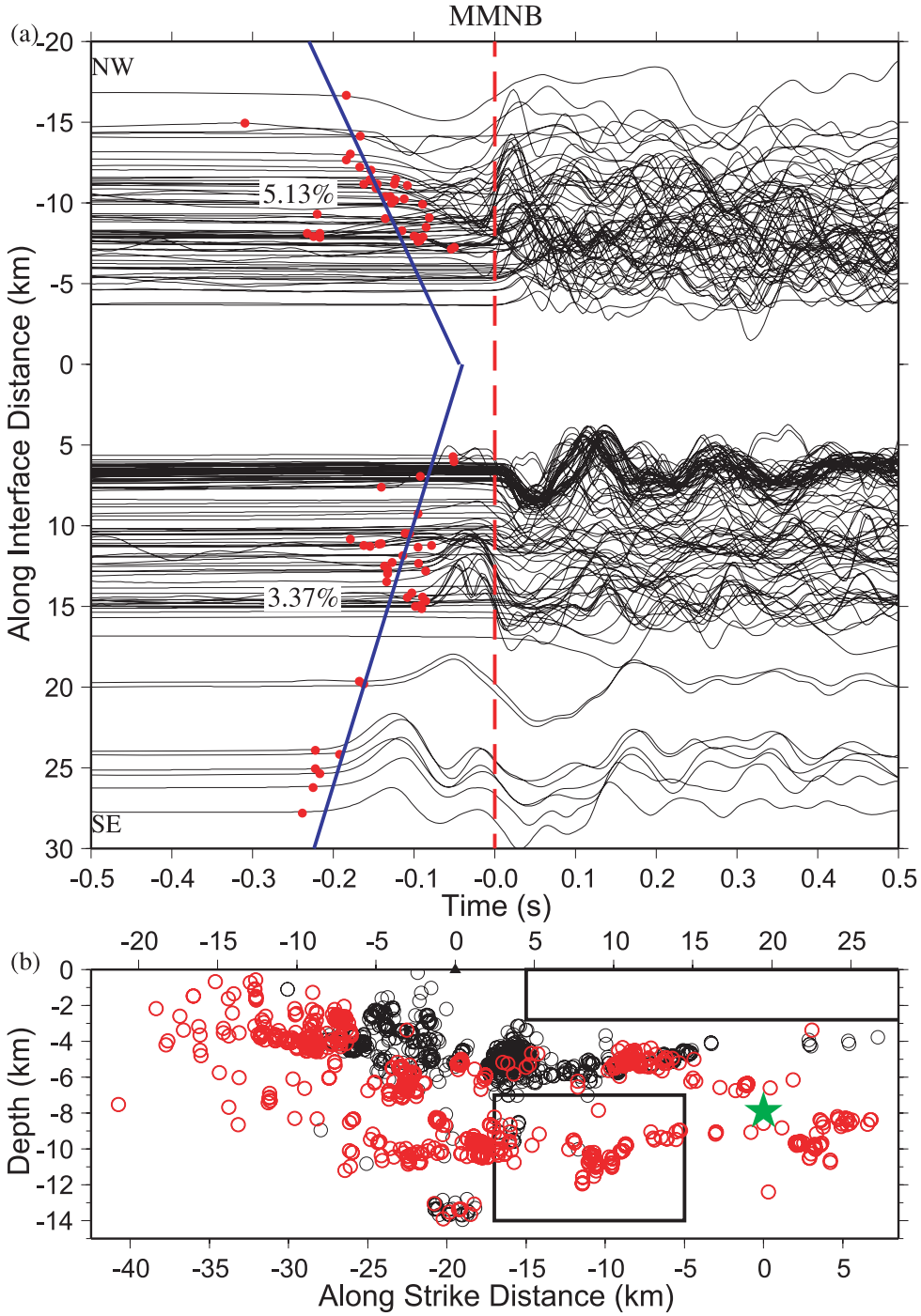

Figure 5. (a) Vertical displacement seismograms recorded by the HRSN station MMNB showing the moveout between FZHW and direct *P* waves along the fault. The red vertical dashed lines mark the onset of the *P* waves. The red dots mark the onset of FZHW and the blue line shows the least-squares fitting of the moveout. The estimated velocity contrasts using eq. (2) and an average *P*-wave velocity of 5.5 km s^{-1} are also labelled. The number of plotted waveforms is reduced by 90 per cent from the analysed data for better illustration. (b) A cross-section view of the seismicity with corresponding waveforms shown in (a) along the 139.2° strike direction. Events with FZHW are marked by red circles. The distances on the top and bottom of the panel are relative to the recording station (black triangle) and the 2004 Parkfield earthquake (the green star) projected along the SAF strike, respectively. The two black rectangles outline the regions with reversed velocity contrast as marked in Fig. 2(c).

Fig. 5 shows clear examples of FZHW at station MMNB that are generated by events to the NW and SE of the station. For events with along-interface distances larger than ∼7 km, the polarities of the first arrival phases are opposite to those predicted for right-lateral focal solutions, as expected for FZHW. In addition, the differential arrival time between FZHW and direct *P* waves increases generally with the along-interface distance. We fit the moveout with the least-squares method and estimate the velocity contrast based on the slope of the moveout using eq. (2). As in Ben-Zion & Malin (1991), we use 5.5 km s^{-1} as the average *P*-wave velocity

in eq. (2). This is consistent with the average value of seismic velocities at seismogenic depth based on the 3-D velocity model of Thurber *et al.* (2006). The estimated average velocity contrasts are ∼5.1 and ∼3.3 per cent for the fault sections to the NW and SE of station MMNB, respectively. In the next three sections, we perform similar analysis using data that are recorded at different stations, and derive detailed results for spatial variations of the velocity contrast in different subsections of the SAF at Parkfield.

5 VARIATIONS OF THE VELOCITY CONTRAST ALONG THE STRIKE OF THE SAF

The identification (or absence) of FZHW associated with given source–receiver geometries can be used to infer on the existence (or absence) of a sharp velocity contrast across the fault in the study region. For example, station CRAB north of MMNB belongs to the

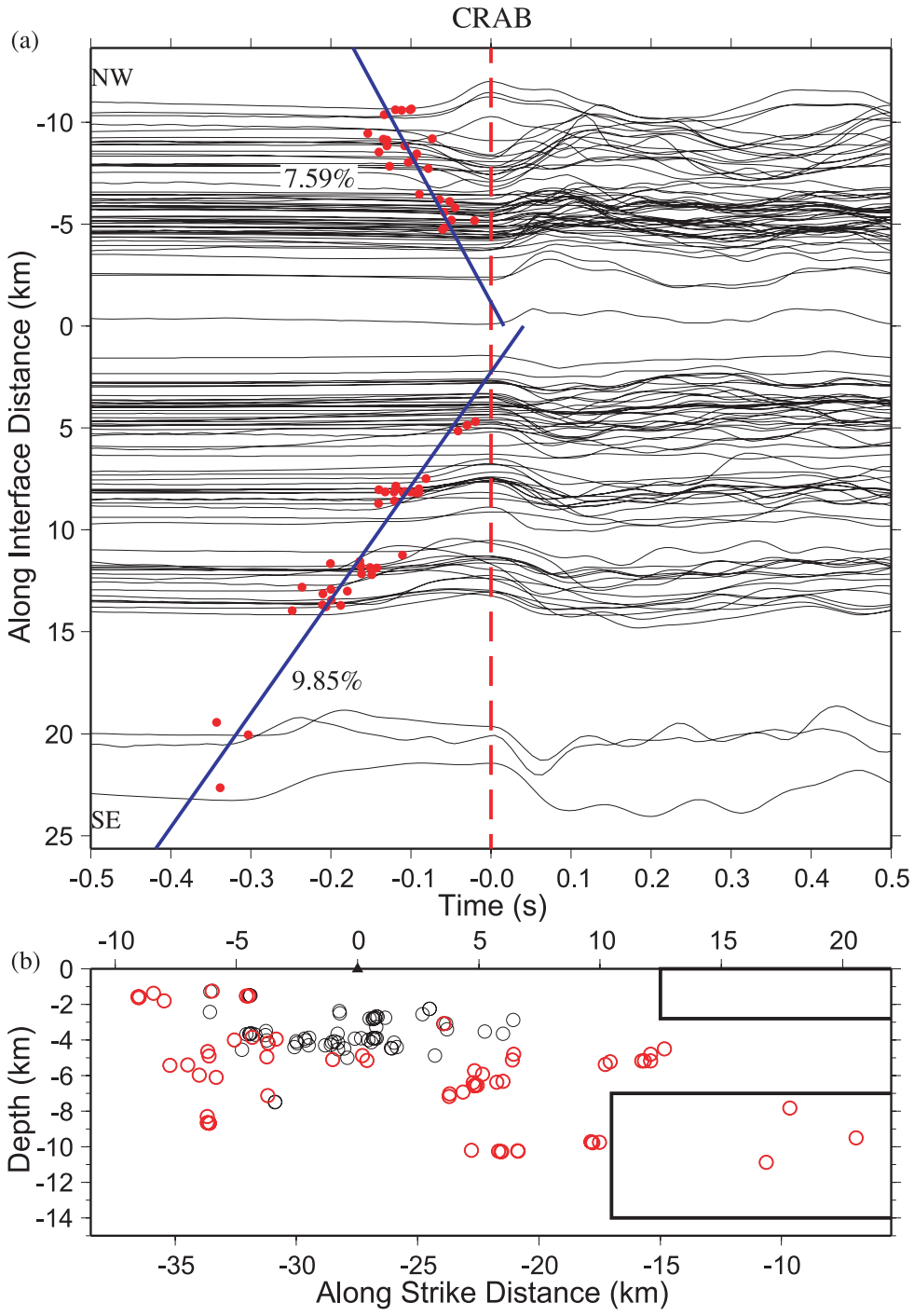

Figure 6. Vertical displacement seismograms recorded by the PASO station CRAB showing the moveout between FZHW and direct *P* waves along the fault. Other symbols are the same as in Fig. 5.

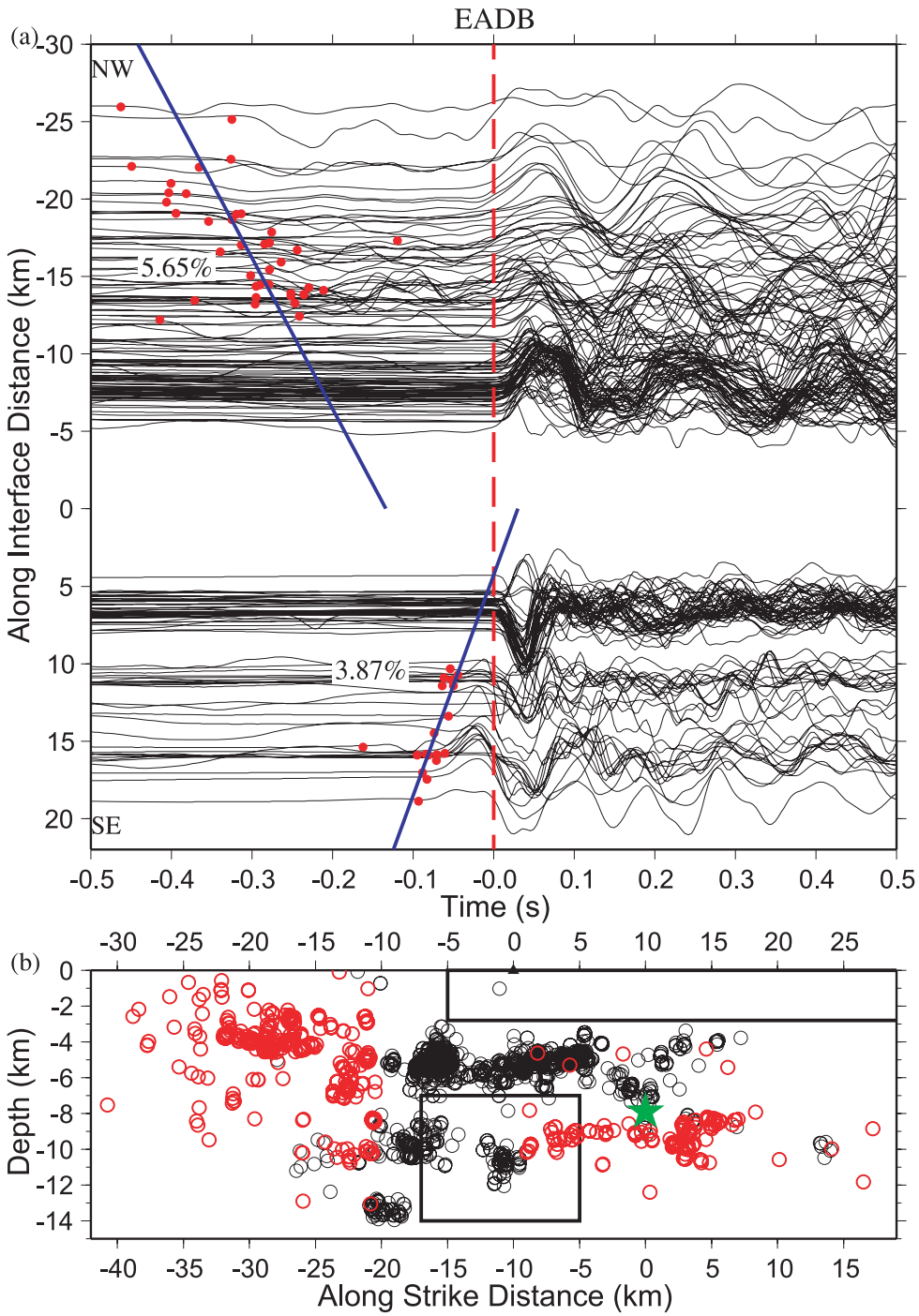

Figure 7. Vertical displacement seismograms recorded by the HRSN station EADB showing the moveout between FZHW and direct *P* waves along the fault. Other symbols are the same as in Fig. 5. The number of waveforms in (a) is reduced by 90 per cent for better illustration.

PASO network, and is located within 1 km of the creeping section of the SAF and approximately 3.2 km north of the SAFOD site (Fig. 1). Clear head waves are observed at this station for events in the NW and SE along-strike directions (Fig. 6). Using an average *P*-wave velocity of 5.5 km s^{-1}, the moveout corresponds to an average velocity contrast of ∼7.6 and ∼9.9 per cent for the fault sections to the NW and SE of station CRAB, respectively. Similarly, Fig. 7 shows clear head wave signals recorded at the HRSN borehole station EADB between stations MMNB and GHIB (Fig. 1). However, the estimated velocity contrasts for sections centred at this station, obtained by the same procedure, are about 5.7 per cent to the NW and only 3.9 per cent to the SE. In addition, the absolute differential arrival times between the FZHW and direct *P* waves from the NW are considerably larger than those from the SE, indicating a possible change of velocity contrast near EADB.

Fig. 8 gives a summary of the velocity contrast values that are derived for sections to the NW and SE that are centred at different stations in the study area. Clear head waves are only observed at stations located NE of the fault, indicating that the seismic velocity on the SW side of the fault is overall faster than that on the NE side.

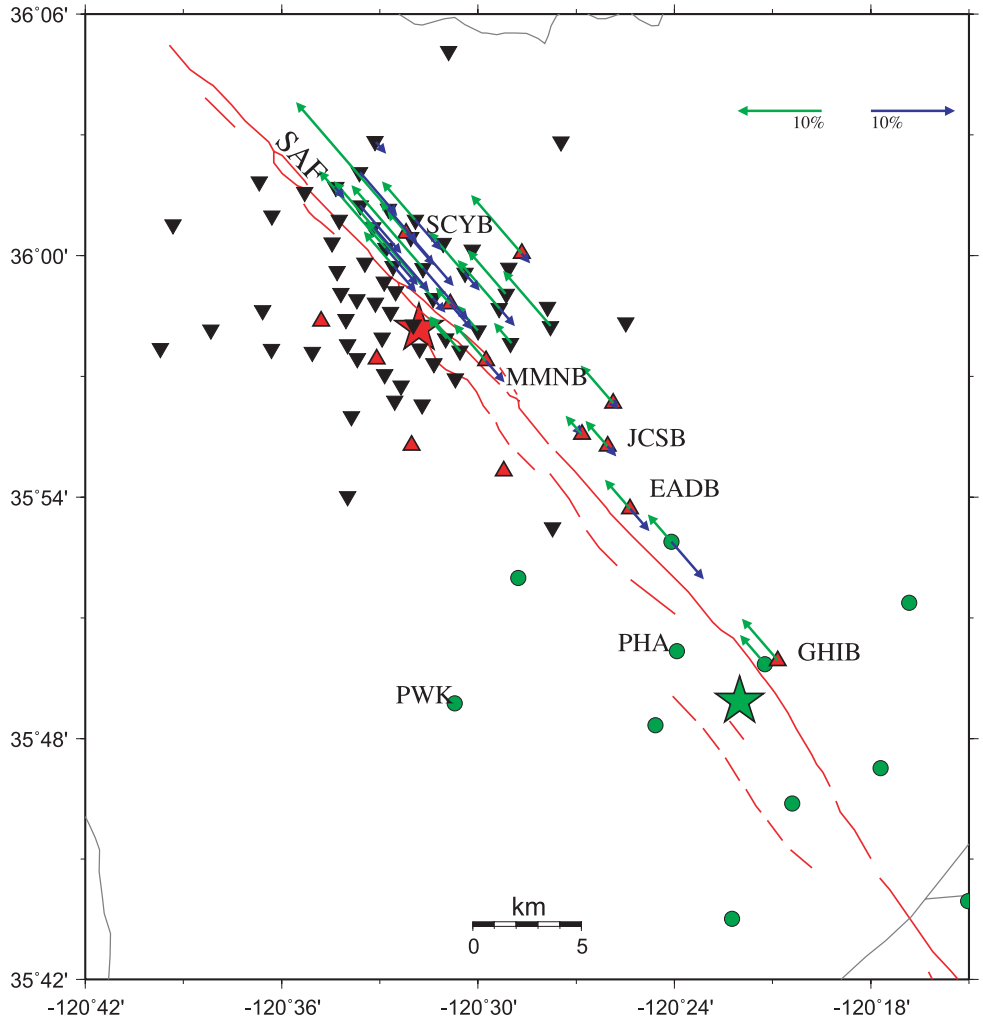

Figure 8. A summary of the obtained velocity contrasts across the SAF in the Parkfield area. The green and blue arrows represent, respectively, velocity contrast values for along-strike sections to the NW and SE that are centred at different stations. The length of each arrow is proportional to the percentage of the velocity contrast. Other symbols are the same as in Fig. 1.

As shown in Fig. 8, however, the results also indicate clear variations of the velocity contrast along the fault. The general pattern is that the velocity contrast reaches its maximum value to the NW of MM (5–10 per cent) and starts decreasing towards the SE. Near the epicentre of the 2004 Parkfield earthquake (i.e. GH), the estimated velocity contrast is very small (0–2 per cent). Additional results on the velocity contrasts at different depths, and in the opposite along-strike directions around GH, are given in Sections 6 and 7.

6 VARIATIONS OF THE VELOCITY CONTRAST WITH HYPOCENTRAL DEPTH

We observe the existence of velocity contrast across the fault throughout the seismogenic zone, along with changes of the velocity contrast with depth and with different locations along the fault. Fig. 9(a) shows a clear moveout of differential arrival times with increasing depth for events having along-strike distances from station MMNB of less than 2 km. Assuming again that the average *P*-wave velocity is 5.5 km s^{-1}, the average velocity contrast for the entire seismogenic zone in that location is ∼7.3 per cent. This value is compatible with the inference of a deep penetrating fault interface near MM from 3-D tomography (Thurber *et al.* 2006) and previous FZHW studies (Ben-Zion *et al.* 1992). In contrast, for events directly beneath station GHIB, which is located close to the epicentre of the 2004 M6 event, we can only identify candidate FZHW in several traces (Fig. 9b). The results imply a lack of a velocity contrast (in which the NE side is the block with slower seismic velocity) over much of the seismogenic zone beneath GHIB.

To obtain additional results on values of the velocity contrasts in the GH region, we plot in Figs 10 and 11 the moveout of FZHW in waveforms at station GHIB that are generated by earthquakes at different depth sections. We separate the entire data set into two groups associated with earthquakes above and below 7 km, which is roughly the boundary between two major near-horizontal seismic streaks identified from relocated seismicity (Waldhauser *et al.* 2004; Thurber *et al.* 2006). Compared with the results around MM near the epicentres of the 1934 and 1966 M6 events (Figs 5 and 9a), the pattern of velocity contrast around GH near the epicentre of the 2004 M6 event exhibits a strong along-strike asymmetry. A clear moveout is shown to the NW side of station GHIB for both shallow and deep seismicity, especially for events that are north of MM (at along-strike distance of about—20 km). This is generally consistent with our previous observations that the velocity contrast is strongest

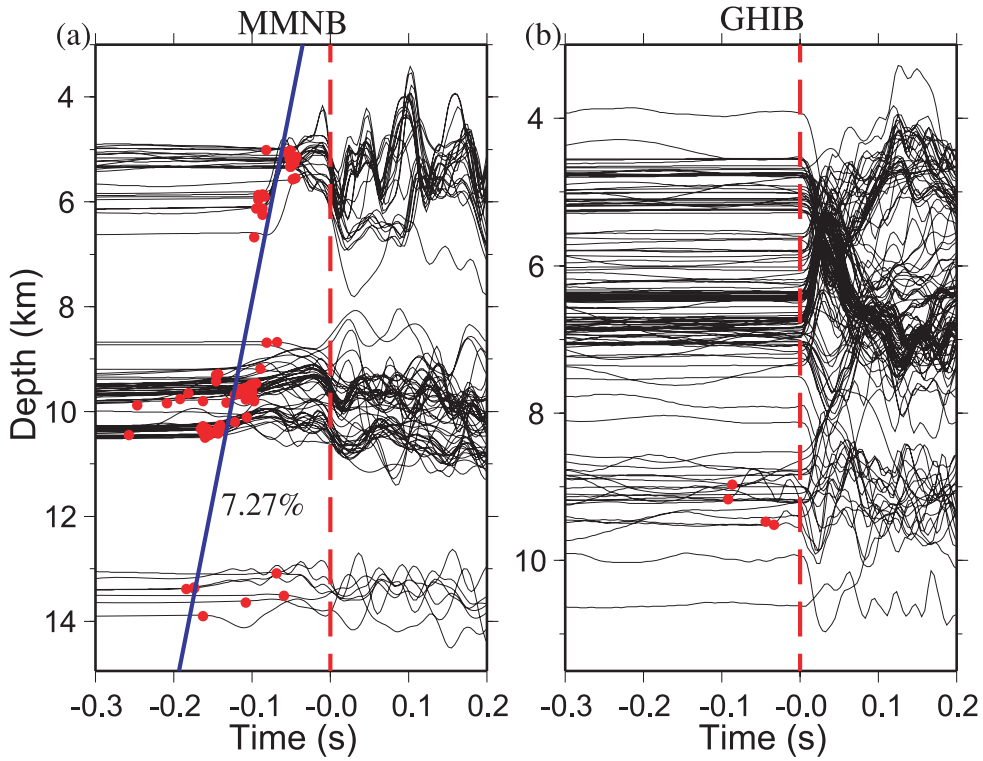

Figure 9. (a) Vertical displacement seismograms recorded at the HRSN station MMNB showing the moveout between FZHW and direct *P* waves with increasing hypocentral depth. The employed events are approximately underneath the station. Other symbols are the same as in Fig. 5. (b) Vertical displacement seismograms recorded at the HRSN station GHIB for events approximately underneath the station. Other symbols are the same as (a).

north of MM and decreases towards GH (Section 5). However, a striking feature of Figs 10 and 11 is the near absence of FZHW at station GHIB from seismicity to the SE section of the fault. This is especially pronounced in Fig. 10, indicating the lack of or very small velocity contrast in the shallow portion of the fault at that section. Even for the seismicity in the deeper part of the fault to the SE of GHIB, head waves can only be observed sparsely from certain locations (Fig. 11), rather than continuously as shown at the stations to the NW. These results demonstrate clear variations in the strength of the velocity contrast near the epicentral region of the 2004 Parkfield earthquake in both along-strike and downdip directions.

7 POSSIBLE REVERSAL OF VELOCITY CONTRAST BETWEEN MM AND GH

As mentioned in Section 2, Eberhart-Phillips & Michael (1993) and Thurber *et al.* (2006) observed a high *P*-wave velocity rock on the (nominally slow) NE side of the SAF at seismogenic depth (Fig. 2). If this high-velocity body is very close to or directly in contact with the active SAF, as suggested by Thurber *et al.* (2006), it will produce a locally reversed velocity contrast. This could generate FZHW that will be recorded at stations on the SW side (generally considered as the fast side) that are within the critical distance x_c for a given along-fault propagation distance (Fig. 3).

To test the possibility of a local reversal of the velocity contrast, we examine waveforms recorded at six NCSN stations on the SW side of the fault near GH (Fig. 1) for systematic opposite first motion polarities. Fig. 12 shows records from station PHA, which is the closest station to the fault on the SW side. The first motions generally match the expected polarities of the direct *P* waves from right-lateral strike-slip focal mechanisms, even for events near the local high velocity region NE of the fault imaged by Thurber *et al.* (2006). The only exception is one cluster of events at depth around 14 km, which are outside the 'suspected' region. However, the abnormal first arrivals from this cluster are unlikely to be associated with FZHW since their focal mechanisms contain a mixture of strike-slip and normal faulting (Fig. 13). We also observe abnormal first motions from this cluster of events at all six stations on the SW side of the SAF. We conclude that the abnormal first motions from this cluster are probably caused by different focal mechanisms in a region of complex source geometries.

Based on the lack of observation of FZHW at station PHA, we can attempt to estimate the upper-limit value of the possible reversed velocity contrast from the local high velocity region NE of the SAF (Fig. 2). Using in eq. (1) and Fig. 3, a normal distance of station PHA from the SAF of 2 km and an average propagation distance of 10 km, the corresponding limit for a reversed velocity contrast is 2 per cent. This estimate assumes that the seismicity is located on the interface between the high velocity body of Fig. 2 and the main SAF. However, the seismicity is clearly offset from the SAF and occurs essentially under the SWFZ. This limits our ability to constrain the maximum allowable value of a sharp reversed velocity contrast of the localized high velocity body NE of the SAF that is imaged by Eberhart-Phillips & Michael (1993) and Thurber *et al.* 2006).

8 DISCUSSION

We conducted a comprehensive imaging of the existence and average properties of sharp velocity contrast interfaces along the Parkfield section of the SAF using FZHW and direct *P* waves. Clear

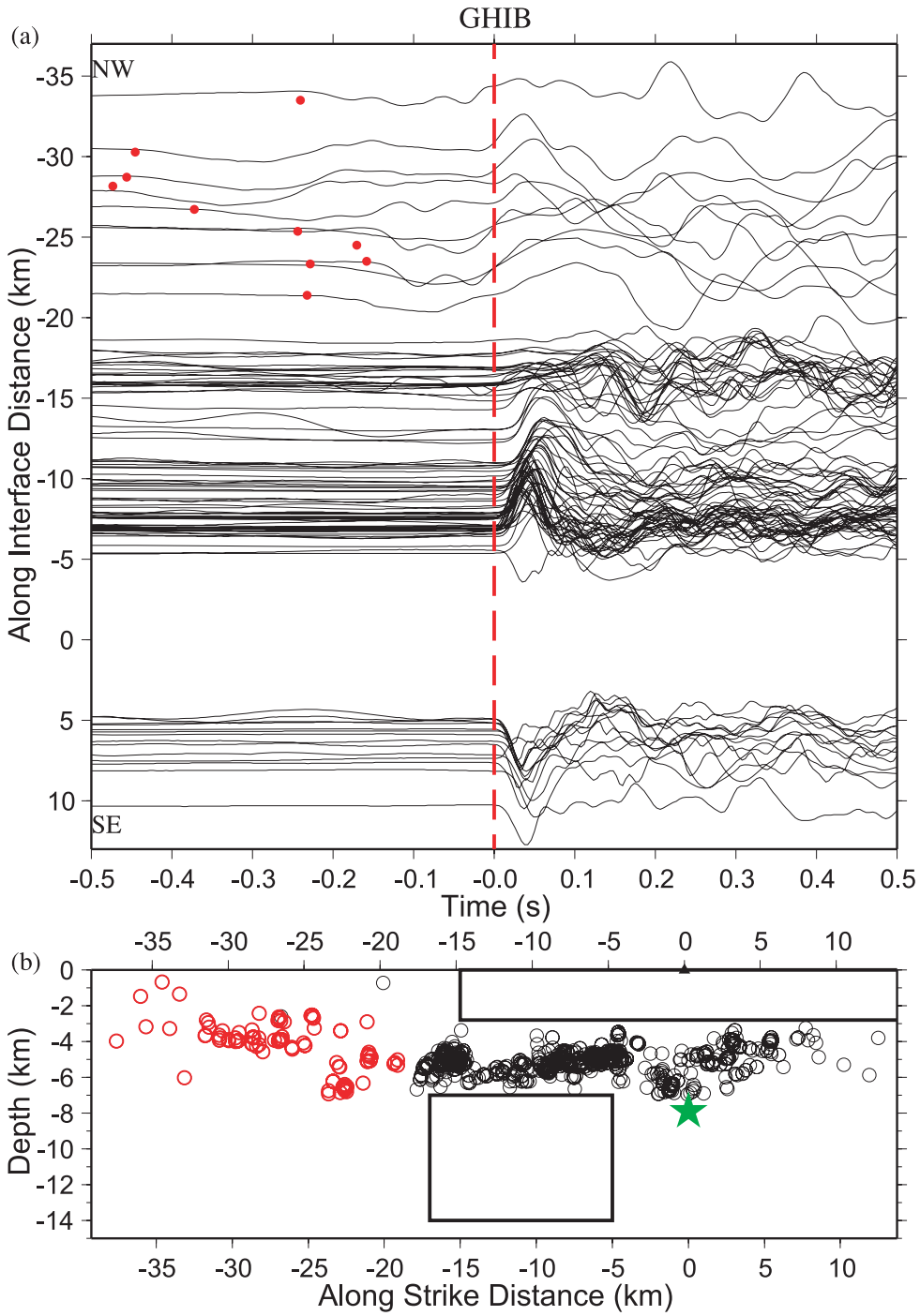

Figure 10. Vertical displacement seismograms recorded by the HRSN station GHIB for earthquakes with hypocentre depths less than 7 km. Other symbols are the same as in Fig. 5. The number of waveforms in (a) is reduced by 75 per cent for better illustration.

FZHW are observed only for stations on the NE side of the fault, indicating that the crustal block to the SW of the fault has generally higher seismic velocity than the block to the NE. In addition, we found clear along-strike variations of the velocity contrast across the SAF (Fig. 8). In the NW part of our study region, and around MM near the epicentres of the 1934 and 1966 M6 events, the velocity contrast is fairly strong (5–10 per cent) and the bimaterial interface extends to the bottom of seismogenic zone (Figs 5 and 9a). On the other hand, around GH near the epicentre of the 2004 M6 Parkfield earthquake the velocity contrast is either absent or very small (0–2 per cent), especially in the top 7 km and in the region to the SE of GH (Figs 9b, 10 and 11).

Our results are generally consistent with the regional geological setting that the Salinian granite on the SW side of the fault has a faster seismic velocity than the Franciscan rock and Great Valley sequence on the NE side. Previous local tomography results also show that the SAF around Parkfield has a clear velocity contrast that varies along the SAF strike (e.g. figs 2c and 6 in Eberhart-Phillips & Michael 1993). We note that the velocity contrasts around MM obtained from previous tomographic results (e.g. Thurber *et al.*

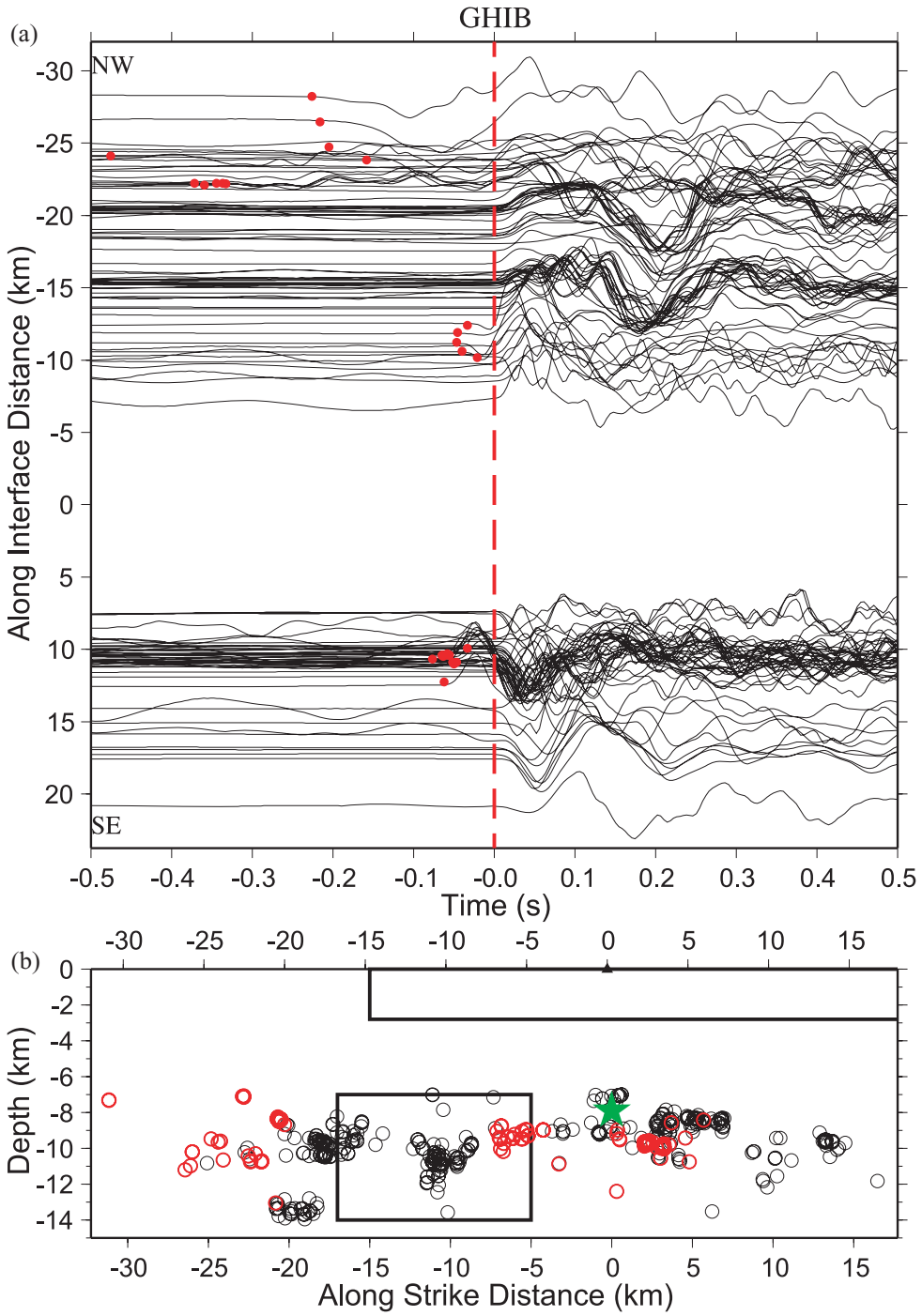

Figure 11. Vertical displacement seismograms recorded by the HRSN station GHIB for earthquakes with hypocentre depths larger than 7 km. Other symbols are the same as in Fig. 5. The number of waveforms in (a) is reduced by 90 per cent for better illustration.

2006) are on the order of 10–30 per cent, which is larger than the range of 5–10 per cent inferred from this study. The difference may be related to the fact that the tomographic images involve rock volumes that extend some distance away from the fault, and may hence be influenced by off-fault structures, while the imaging based on FZHW apply more strictly to the fault interface itself. It is also possible that the along-strike spatial averaging of FZHW as they propagate through regions with different velocity contrasts may reduce the obtained contrast values.

The geological observation of mafic igneous rocks, local seismic tomography results, and local gravity map all indicate the existence of high-velocity rocks on the NE side of the fault near GH (Eberhart-Phillips & Michael 1993; McPhee *et al.* 2004; Thurber *et al.* 2006). Some of these studies suggest that the seismic velocity of these rocks on the NE side may exceed that of the predominantly faster rock to the SW of the fault (Fig. 2c), producing a locally reversed velocity contrast across the SAF. Unfortunately, the locations of the seismicity and stations on the SW side of the fault limit our ability

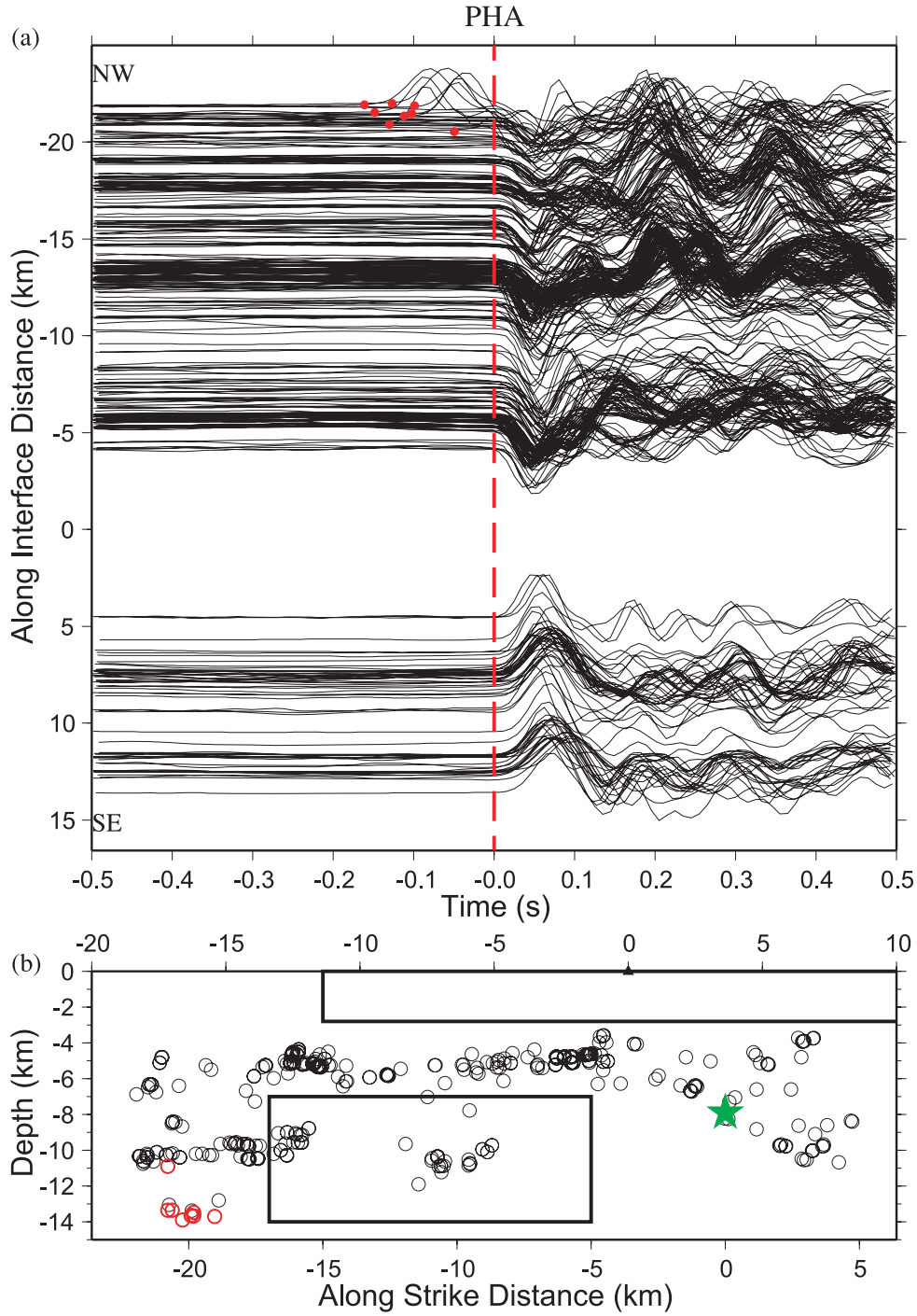

Figure 12. (a) Vertical displacement seismograms recorded at the HRSN station PHA located SW of the fault. Waveforms with first motions opposite to the polarities predicted from right-lateral focal mechanisms are marked by red dots. (b) The seismicity with corresponding waveforms shown in (a) along the 139.2° strike. Events with abnormal first motions in (a) are shown with red circles. Other symbols are the same as Fig. 5.

to confirm the existence of a sharp reversed velocity contrast across the SAF in that area. We may infer that the high-velocity rock on the NE side of the SAF near GH probably does not touch the SWFZ, which is outlined by the active seismicity, at seismogenic depth, and the rocks adjacent to SWFZ on both sides probably have the same seismic velocities in that region.

The along-strike variations of the velocity contrast observed in this study are consistent with geological and geophysical results on the evolution of the SAF in this region. Detailed geological studies have found mafic igneous rocks exposed at GH on the NE side of the main SAF surface trace, which may correspond to the high-velocity body imaged by previous tomography studies (e.g. Eberhart-Phillips & Michael 1993; Thurber *et al.* 2006). These rocks have similar characteristics to those exposed at the Eagle Rest Peak about 150 km to the SE, and hence were likely transported to GH (e.g. Sims 1993) by the movement of the Pacific Plate. Simpson *et al.* (2006) suggested that the presence of these rocks on the 'wrong' side of the SAF is consistent with progressive northeastward bending of

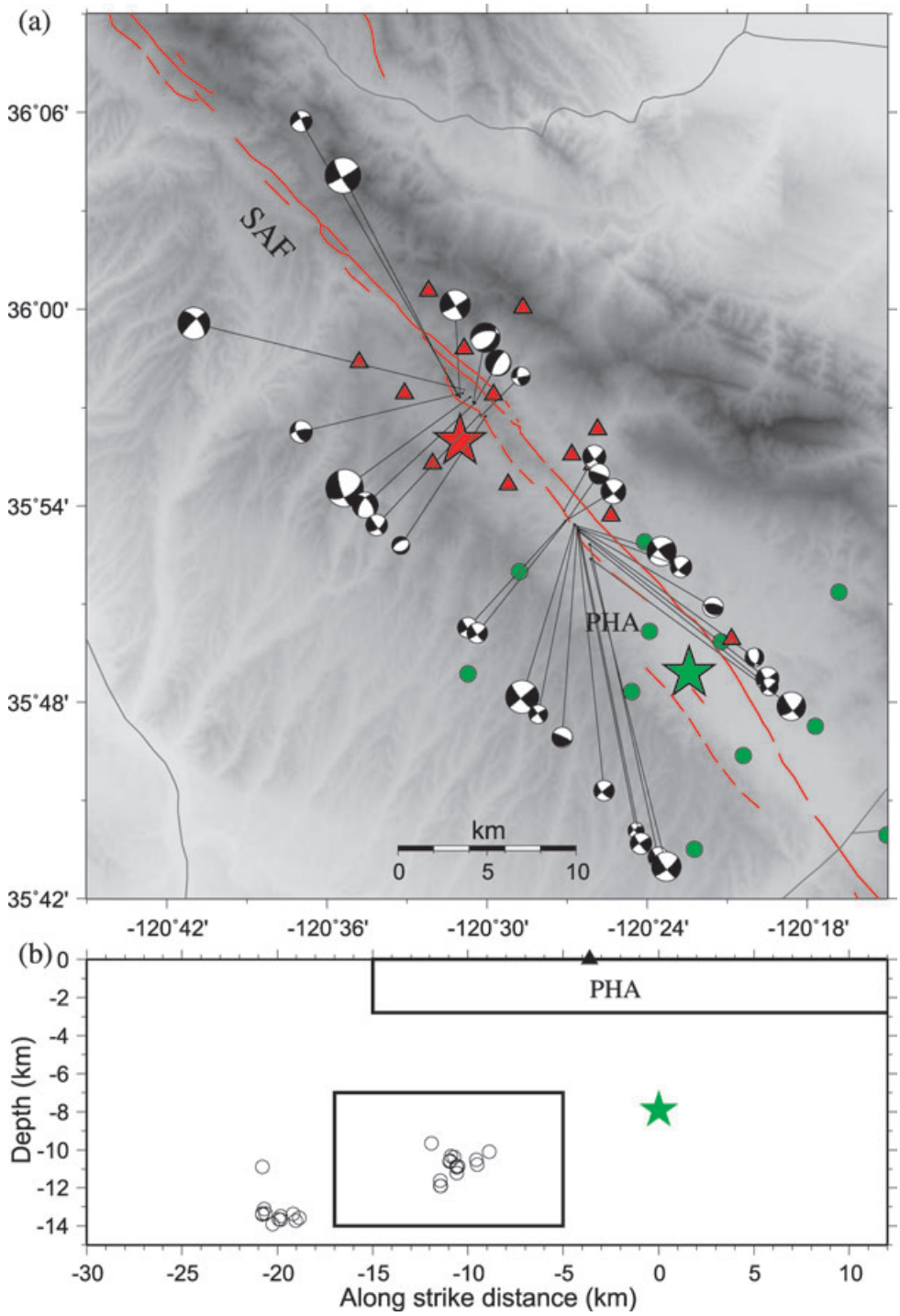

Figure 13. Focal mechanism solutions of selected events from the 'suspected' region with reversed velocity contrast and the events marked in Fig. 12 with red circles. Other symbols are the same as Fig. 5. The focal mechanism solutions are obtained from the Northern California Earthquake Data Center.

the SAF and development of a new fault interface (e.g. SWFZ) with time around Parkfield. This could move rocks that were previously on the SW (i.e. overall faster) side of the fault to the NE side of the 'new' fault interface. Because the largest warp of the fault traces is near GH (fig. 2 of Simpson *et al.* 2006), we should expect that the fault interface near GH has a smaller velocity contrast than that near MM. This is supported by our observations. The multiple shifts of the active traces of the SAF near GH (Dibblee *et al.* 1999) could also offset the newly developing active fault in that area (SWFZ) away from a sharp bimaterial interface. The high-velocity rock on the NE side of the main SAF near GH appears to be seismically inactive at present (e.g. Simpson *et al.* 2006; Thurber *et al.* 2006).

Our observations of clear along-strike variations of the velocity contrast along the SAF offer, along with the above discussion, an explanation for the mixed propagation directions of the M6-type Parkfield earthquakes (Harris & Day 2005; Ben-Zion 2006). Since the velocity contrast around MM is large and positive (with the SW side being fast and the NE side being slow), the preferred

propagation direction for earthquakes nucleating in that region is to the SE. The 1934 and 1966 events had hypocentres around the MM region, and were associated with propagation directions to the SE, which is consistent with the preferred rupture direction generated by the bimaterial effects (e.g. Weertman 1980; Shi & Ben-Zion 2006; Ampuero & Ben-Zion 2008). The 2004 M6 earthquake nucleated near GH with a near-zero velocity contrast in the active seismic fault (i.e. the SWFZ) and perhaps a reversed contrast across the main SAF (e.g. Thurber *et al.* 2006). Thus, in contrast to the region further to the north, the region around the hypocentre of the 2004 event is not expected to produce a preferred propagation direction to the SE. Instead, the discussed local structural complexities would probably dominate the nucleation and propagation of earthquake ruptures near GH.

Our results on the reduction in the strength of the velocity contrast across the SAF near GH also provide a dynamic arrest mechanism for the M6 Parkfield events. This is because the amplitude of the dynamic changes of normal stress along a bimaterial interface increases (e.g. Ben-Zion & Andrews 1998; Ranjith & Rice 2001; Ben-Zion & Huang 2002) with increasing degree of the velocity contrast (at least up to about 30–40 per cent contrast of *S*-wave velocities). Thus, earthquakes that nucleate near MM will encounter during their propagation to the SE increasing frictional strength, due to the diminishing dynamic bimaterial reduction of normal stress associated with the decreasing velocity contrast in the SE section. Similarly, earthquakes that nucleate near GH will encounter with continuing propagation to the NW increasing frictional strength, due to the growing dynamic increase of normal stress at the rupture tip produced by the increasingly pronounced velocity contrast (with slower NE side) in the NW section.

Additional details on the differences between the velocity contrasts across the SAF in the MM and GH regions can be obtained by performing a joint inversion of FZHW and direct *P* waves for dissimilar layered velocity structures on the opposite sides of the fault in these locations (Ben-Zion *et al.* 1992; Lewis *et al.* 2007). This is left for future work.

ACKNOWLEDGMENTS

Most seismograms used in this study were recorded by the High Resolution Seismic Network (HRSN) operated by the Berkeley Seismological Laboratory, University of California, Berkeley, and the Northern California Seismic Network (NCSN) operated by the U.S. Geological Survey, Menlo Park. The data are distributed by the Northern California Earthquake Data Center (NCEDC). We thank Haijiang Zhang for providing the PASO data and the 3-D velocity model of Thurber *et al.* (2006), Jeanne Hardebeck for providing information on focal mechanisms in the Parkfield region, and Andy Michael and Robert Jachens for providing the 3-D geological map for the Parkfield region. The manuscript benefited from useful comments by two anonymous referees and Editor Xiaofei Chen. The study was supported by the National Science Foundation (grant EAR-0844103).

REFERENCES

Abercrombie, R.E., 1996. The magnitude-frequency distribution of earthquakes recorded with deep seismometers at Cajon Pass, southern California, *Tectonophysics,* **261,** 1–7.

Adams, G.G., 1995. Self-excited oscillations of two elastic half-spaces sliding with constant coefficient of friction, *J. appl. Mech.,* **62,** 867–872.

Aki, K. & Richards, P.G., 2002. *Quantitative Seismology* 2nd edn, University Science Books, Sausalito, CA.

Ampuero, J.-P. & Ben-Zion, Y., 2008. Cracks, pulses and macroscopic asymmetry of dynamic rupture on a bimaterial interface with velocity-weakening friction, *Geophys. J. Int.,* **173**(2), 674–692, doi:10.1111/j.1365-246X.2008.03736.x.

Andrews, D.J. & Ben-Zion, Y., 1997. Wrinkle-like slip pulse on a fault between different materials, *J. geophys. Res.,* **102,** 553–571.

Bakun, W.H. & Lindh, A.G., 1985. The Parkfield, California, earthquake prediction experiment, *Science,* **229,** 619–624.

Bakun, W.H. *et al*., 2005. Implications for prediction and hazard assessment from the 2004 Parkfield earthquake, *Nature,* **437,** 969–974, doi:10.1038/nature04067.

Ben-Zion, Y., 1989. The response of two joined quarter spaces to SH line sources located at the material discontinuity interface, *Geophys. J. Int.,* **98,** 213–222.

Ben-Zion, Y., 1990. The response of two half spaces to point dislocations at the material interface, *Geophys. J. Int.,* **101,** 507–528.

Ben-Zion, Y., 2001. Dynamic ruptures in recent models of earthquake faults. *J. Mech. Phys. Solids,* **49,** 2209–2244.

Ben-Zion, Y., 2003. Appendix 2, Key Formulas in Earthquake Seismology, in *International Handbook of Earthquake and Engineering Seismology, Part B*, pp. 1857–1875, eds Lee, W.H.K., Kanamori, H., Jennings, P.C. & Kisslinger, C., Academic Press.

Ben-Zion, Y., 2006. A comment on "Material contrast does not predict earthquake rupture propagation direction" by R. A. Harris and S. M. Day, *Geophys. Res. Lett.,* **33,** L13310, doi:10.1029/2005GL025652.

Ben-Zion, Y. & Aki, K., 1990. Seismic radiation from an SH line source in a laterally heterogeneous planar fault zone, *Bull. seism. Soc. Am.,* **80,** 971–994.

Ben-Zion, Y. & Andrews, D.J., 1998. Properties and implications of dynamic rupture along a material interface, *Bull. seism. Soc. Am.,* **88,** 1085–1094.

Ben-Zion, Y. & Huang, Y., 2002. Dynamic rupture on an interface between a compliant fault zone layer and a stiffer surrounding Solid, *J. geophys. Res.,* **107**(B2), doi:10.1029/2001JB000254.

Ben-Zion, Y. & Malin, P., 1991. San Andreas fault zone head waves near Parkfield, California, *Science,* **251,** 1592–1594.

Ben-Zion, Y., Katz, S. & Leary, P., 1992. Joint inversion of fault zone head and direct P arrivals for crustal structure near major faults, *J. geophys. Res.,* **97,** 1943–1951.

Brietzke, G.B. & Ben-Zion, Y., 2006. Examining tendencies of in-plane rupture to migrate to material interfaces, *Geophys. J. Int.,* **167,** 807–819, doi:10.1111/j.1365-246X.2006.03137.x.

Brietzke, G.B., Cochard, A. & Igel, H., 2007. Dynamic rupture along bimaterial interfaces in 3D, *Geophys. Res. Lett.,* **34,** L11305, doi:10.1029/2007GL029908.

Brietzke, G.B., Cochard, A. & Igel, H., 2009. Importance of bimaterial interfaces for earthquake dynamics and strong ground motion, *Geophys. J. Int.,* **178**(2), 921–938.

Brown, R.D., Jr. *et al*., 1967. The Parkfield-Cholame, California, earthquakes of June–August 1966—surface geologic effects, water-resources aspects, and preliminary seismic data, *U.S. Geol. Surv. Prof. Paper,* **579,** 66.

Catchings, R.D., Rymer, M.J., Goldman, M.R., Hole, J.A., Huggins, R. & Lippus, R., 2002. High-resolution seismic velocities and shallow structure of the San Andreas fault zone at Middle Mountain, Parkfield, California, *Bull. seism. Soc. Am.,* **92,** 2493–2503.

Dalguer, L.A. & Day, S.M., 2007. Asymmetric pulse-like rupture at bimaterial interface with slip-weakening friction model, *EOS, Trans. Am. geophys. Un., Fall Meet. Suppl.,* **88**(52), Abstract S14B–03.

Dibblee, T.W., Graham, S.E., Mahony, T.M., Blissenbach, J.L., Mariant, J.J. & Wentworth, C.M., 1999. Regional geological map of San Andreas and related faults in Carrizo Plain, Temblor, Caliente and La Panza Ranges and vicinity, California: a digital database, *U.S. Geol. Surv. Open-File Rept.* 99–14, scale: 1: 125,000.

Eberhart-Phillips, D. & Michael, A.J., 1993. Three-dimensional velocity structure, seismicity, and fault structure in the Parkfield region, central California, *J. geophys. Res.,* **98,** 15 737–15 758.

Eshelby, J.D., 1957. The determination of the elastic field of an ellipsoidal inclusion, and related problems, *Proc. Roy. Soc. Ser. A,* **241,** 376–396.

Fialko, Y., 2006. Interseismic strain accumulation and the earthquake potential on the southern San Andreas fault system, *Nature,* **441,** 968–971.

Fuis, G.S., Ryberg, T., Godfrey, N.J., Okaya, D.A. & Murphy, J.M., 2001. Crustal structure and tectonics from the Los Angeles basin to the Mojave Desert, southern California, *Geology,* **29,** 15–18.

Fuis, G.S. *et al*., 2003. Fault systems of the 1971 San Fernando and 1994 Northridge earthquakes, southern California: relocated aftershocks and seismic images from LARSE II, *Geology,* **31**(2), 171–174.

Harris, R.A., 2004. A scientific hypothesis debunked by parkfield earthquakes–material contrasts and rupture directivity, *EOS, Trans. Am. geophys. Un.,* **85,** S54B-08.

Harris, R.A. & Day, S.M., 2005. Material contrast does not predict earthquake rupture propagation direction, *Geophys. Res. Lett.,* **32,** L23301, doi:10.1029/2005GL023941.

Hickman, S., Zoback, M.D. & Ellsworth, W., 2004. Introduction to special section: preparing for the San Andreas Fault Observatory at Depth, *Geophys. Res. Lett.,* **31,** L12S01, doi:10.1029/2004GL020688.

Hough, S.E., Ben-Zion, Y. & Leary, P., 1994. Fault zone waves observed at the southern Joshua Tree earthquake rupture zone, *Bull. seism. Soc. Am.,* **84,** 761–767.

Langbein, J. *et al*., 2005. Preliminary report on the 28 September 2004, M 6.0 Parkfield, California earthquake, *Seism. Res. Lett.,* **76,** 10–26.

Le Pichon, X., Kreemer, C. & Chamot-Rooke, N., 2005. Asymmetry in elastic properties and the evolution of large continental strike-slip faults, *J. geophys. Res.,* **110,** B03405, doi:10.1029/2004JB003343.

Lees, J.M. & Malin, P.E., 1990. Tomographic images of *P*-wave velocity variation at Parkfield, California, *J. geophys. Res.,* **95**(B13), 21 793–21 804.

Lewis, M.A., Ben-Zion, Y. & McGuire, J.J., 2007. Imaging the deep structure of the San Andreas Fault south of Hollister with joint analysis of fault-zone head and direct *P* arrivals, *Geophys. J. Int.,* doi:10.1111/j.1365-246X.2006.03319.x.

Lindh, A.G. & Boore, D.M., 1981. Control of rupture by fault geometry during the 1966 Parkfield earthquake, *Bull. seism. Soc. Am.,* **71,** 95–116.

Lutter, W.J. *et al*., 2004. Upper crustal structure from the Santa Monica mountains to the Sierra Nevada, southern California: tomographic results from the Los Angeles regional seismic experiment, Phase II (LARSE II), *Bull. seism. Soc. Am.,* **94**(2), 619–632.

McLaughlin, R.J., Sliter, W.V., Sorg, D.H., Russell, P.C. & Sarna-Wojcicki, A.M., 1996. Large-scale right-slip displacement on the east San Francisco Bay region fault system, California: implications for location of late Miocene to Pliocene Pacific plate boundary, *Tectonics* **15,** 1–18.

McGuire, J.J. & Ben-Zion, Y., 2005. High-resolution imaging of the Bear Valley section of the San Andreas fault at seismogenic depths with fault-zone head waves and relocated seismicity, *Geophys. J. Int.,* **163,** 152–164.

McGuire, J.J., Zhao, L. & Jordan, T.H., 2001. Teleseismic inversion for the second-degree moments of earthquake space–time distributions, *Geophys. J. Int.,* **145,** 661–678.

McPhee, D.K., Jachens, R.C & Wentworth, C.M, 2004. Crustal structures across the San Andreas Fault at the SAFOD site from potential field and geologic studies, *Geophys. Res. Lett.,* **31,** L12S03, doi:10.1029/2003GL019363.

Michelini, A. & McEvilly, T.V., 1991. Seismological studies at Parkfield. I. Simultaneous inversion for velocity structure and hypocentres using cubic B-splines parameterization, *Bull. seism. Soc. Am.,* **81,** 524–552.

Olsen, K.B. *et al*., 2006. Strong shaking in Los Angeles expected from southern San Andreas earthquake, *Geophys. Res. Lett.,* **33,** L07305, doi:10.1029/2005GL025472.

Page, B.M., 1981. The southern Coast Ranges, in *The Geotectonic Development of California,* pp. 329–417, ed. Ernst, W.G., Prentice–Hall, New York.

Ranjith, K. & Rice, J.R., 2001. Slip dynamics at an interface between dissimilar materials, *J. Mech. Phys. Solids,* **49,** 341–361.

Rymer, M.J. *et al*., 2006. Surface fault slip associated with the 2004 Parkfield, California, Earthquake, *Bull. seism. Soc. Am.,* **96**(4B), S11–S27.

Shapiro, N.M., Campillo, M., Stehly, L. & Ritzwoller, M.H., 2005. High-resolution surface-wave tomography from ambient seismic noise, *Science,* **307,** 1615–1618, doi:10.1126/science.1108339.

Shi, Z. & Ben-Zion, Y., 2006. Dynamic Rupture on a bimaterial interface governed by slip-weakening friction, *Geophys. J. Int.,* **164,** 469–484, doi:10.1111/j.1365-246X.2006.02853.x.

Shi, Z. & Ben-Zion, Y., 2009. Seismic radiation from tensile and shear point dislocations between similar and dissimilar solids, *Geophys. J. Int.,* **179,** 444–458, doi:10.1111/j.1365-246X.2009.04299.x.

Sieh, K., 1978. Slip along the San Andreas fault associated with the great 1857 earthquake, *Bull. seism. Soc. Am.,* **68,** 1421–1448.

Simpson, R.W., Barall, M., Langbein, J., Murray, J.R. & Rymer, M.J., 2006. San Andreas fault geometry in the Parkfield, California, region, *Bull. seism. Soc. Am.,* **96**(4B), S28–S37.

Thurber, C.H., Roecker, S., Roberts, K., Gold, M., Powell, L. & Rittger, K., 2003. Earthquake locations and three-dimensional fault zone structure along the creeping section of the San Andreas Fault near Parkfield, CA: preparing for SAFOD, *Geophys. Res. Lett.,* **30,** doi:10.1029/2002GL016004.

Thurber, C.H., Roecker, S., Zhang, H., Baher, S. & Ellsworth, W., 2004. Fine-scale structure of the San Andreas fault and location of the SAFOD target earthquakes, *Geophys. Res. Lett.* **31,** L12S02, doi:10.1029/2003GL019398.

Thurber, C.H., Zhang, H., Waldhauser, F., Hardebeck, J., Michael, A. & Eberhart-Phillips, D., 2006. Three-dimensional compressional wavespeed model, earthquake relocations, and focal mechanisms for the Parkfield, California, region, *Bull. seism. Soc. Am.,* **96**(4B), S38–S49, doi:10.1785/0120050825.

Waldhauser, F., Ellsworth, W.L., Schaff, D.P. & Cole, A., 2004. Streaks, multiplets, and holes: high-resolution spatio-temporal behavior of Parkfield seismicity, *Geophys. Res. Lett.,* **31,** L18608, doi:10.1029/2004GL020649.

Walter, A.W. & Mooney, W.D., 1982. Crustal structure of the Diablo and Gabilain ranges central California; a reinterpretation of existing data, *Bull. seism. Soc. Am.,* **72,** 1567–1590.

Wdowinski, S., Smith-Konter, B., Bock, Y. & Sanwell, D., 2007. Diffuse interseismic deformation across the Pacific-North America plate boundary, *Geology,* **35**(4), 311–314.

Weertman, J., 1980. Unstable slippage across a fault that separates elastic media of different elastic constants, *J. geophys. Res.,* **85,** 1455–1461.

Weertman, J., 2002. Subsonic type earthquake dislocation moving at approximately $\sqrt{2}\times$ shear wave velocity on interface between half spaces of slightly different elastic constants, *Geophys. Res. Lett.,* **29**(10), doi:10.1029/2001GL013916.

Zhao, P. & Peng, Z., 2008. Velocity contrast along the Calaveras fault from analysis of fault zone head waves generated by repeating earthquakes, *Geophys. Res. Lett.,* **35,** L01303, doi:10.1029/2007GL031810.